Journal of Alloys and Compounds 545 (2012) 200–209

Contents lists available at SciVerse ScienceDirect

Journal of Alloys and Compounds

journal homepage: www.elsevier.com/locate/jalcom

Synthesis and properties of iridium-doped hematite (α-Fe_2O_3)

Stjepko Krehula [a,*], Goran Štefanić [a], Krešo Zadro [b], Ljerka Kratofil Krehula [c], Marijan Marciuš [a], Svetozar Musić [a]

[a] Division of Materials Chemistry, Ruđer Bošković Institute, P.O. Box 180, HR-10002 Zagreb, Croatia
[b] Department of Physics, Faculty of Science, University of Zagreb, Bijenička 32, 10000 Zagreb, Croatia
[c] Faculty of Chemical Engineering and Technology, University of Zagreb, Marulićev trg 19, 10000 Zagreb, Croatia

ARTICLE INFO

Article history:
Received 13 June 2012
Received in revised form 1 August 2012
Accepted 3 August 2012
Available online 10 August 2012

Keywords:
Hematite
Iridium
Morin transition
^{57}Fe Mössbauer
UV–Vis–NIR

ABSTRACT

The effect of the incorporation of Ir^{3+} ions on the properties of α-Fe_2O_3 formed by dehydroxylation of α-FeOOH was investigated using X-ray powder diffraction (XRD), thermogravimetric analysis (TGA), ^{57}Fe Mössbauer, UV–Vis–NIR and FT-IR spectroscopies, SQUID magnetometer, field emission scanning electron microscopy (FE-SEM) and energy dispersive X-ray spectroscopy (EDS). Pure and Ir-doped hematite samples were obtained by heating of pure and Ir-doped goethites (α-FeOOH) formed by precipitation from mixed Fe(III)–Ir(III) chloride solutions in a highly alkaline medium. The incorporation of Ir^{3+} ions into the α-Fe_2O_3 structure led to changes in unit-cell dimensions, crystallinity, particle size and shape, as well as changes in the magnetic, infrared and UV–Vis properties. An increase in the temperature of the Morin transition with an increase in Ir-doping was observed by Mössbauer spectroscopy and magnetic measurements.

1. Introduction

Hematite (α-Fe_2O_3), the most stable iron oxide under ambient conditions, is an important compound which is abundant in nature and has various technological applications [1]. It crystallizes in a trigonal crystal system, space group $R\bar{3}c$. A unit cell can be presented as hexagonal ($a = 5.038$ Å, $c = 13.772$ Å) [2] or rhombohedral ($a = 5.427$ Å, $\alpha = 55.3°$) [1]. The structure is based on the hexagonal close-packed planes of O^{2-} anions stacked along the hexagonal [001] or rhombohedral [111] axis with the Fe^{3+} cations occupying two-thirds of the octahedral sites [1,3].

The doping of α-Fe_2O_3 by various metal cations has been extensively investigated [4–23] due to the relevance of such materials to natural processes as well as their suitability for a number of existing and potential applications (pigments, catalysts, gas sensors, photoanodes for photoelectrochemical water splitting). Hematite doping by selected cations can bring about a change in color [1,24–26], a change in magnetic properties [3,27–33], improvement of catalytic properties [34,35], a large increase in gas-sensitivity [36–38], electrical conductivity [39,40] and photocurrent density [41–46], which is crucial for hematite application in water photooxidation.

Iron oxide doping by iridium has been much less investigated, in spite of a significant potential of Ir^{3+}-for-Fe^{3+} substitution (the same charge and similar radii). Liu [30] investigated the magnetic properties of hematite doped with Ir^{4+} ions and observed an abrupt increase in the Morin transition temperature even for small iridium substitutions. Punnoose et al. [47] investigated the magnetic properties of Ir-doped ferrihydrite nanoparticles and concluded that Ir-for-Fe substitution occurs primarily at the surface of ferrihydrite nanoparticles. Berry et al. [48,49] investigated titania-supported iron(III)–iridium(III) catalysts in situ by ^{57}Fe Mössbauer spectroscopy. By means of different impregnation sequences Zhang et al. [50] prepared the $IrFeO_x/SiO_2$ catalyst which was very active and selective for preferential CO oxidation in a H_2-rich atmosphere. Hematite with surface-deposited IrO_2 particles (as a water oxidation catalyst) showed promising results (high photocurrent density) for light-induced water splitting [51].

In our previous work by Krehula and Musić [52] the formation of iron oxides in a highly alkaline medium in the presence of Ir^{3+} ions was investigated. A strong influence of these ions on the precipitation of solid phases as well as their incorporation into the structures of α-FeOOH and α-Fe_2O_3 was noticed. An increase in the temperature of magnetic transition (Morin transition) by incorporation of Ir^{3+} ions into α-Fe_2O_3 was observed by Mössbauer spectroscopy. In order to elucidate the properties of Ir-doped hematite in more detail, we prepared a series of hematites doped with Ir^{3+} ions and analyzed their properties by applying various instrumental techniques.

---

[*] Corresponding author. Tel.: +385 1 4561 094; fax: +385 1 4680 098.
E-mail address: krehul@irb.hr (S. Krehula).

0925-8388/$ - see front matter © 2012 Elsevier B.V. All rights reserved.
http://dx.doi.org/10.1016/j.jallcom.2012.08.009

2. Experimental

2.1. Sample preparation

Pure and Ir-doped α-Fe_2O_3 particles were prepared by heating uniform lath-like α-FeOOH and Ir-doped α-FeOOH particles synthesized by an original method reported in our previous publications [53,54]. Iron(III) chloride hexahydrate ($FeCl_3\cdot 6H_2O$) of analytical purity, supplied by *Kemika*, iridium(III) chloride ($IrCl_3$) and a tetramethylammonium hydroxide (TMAH) solution (25% w/w, electronic grade 99.9999%) supplied by *Alfa Aesar*® were used. Twice-distilled water prepared in our own laboratory was used in all experiments. Predetermined volumes of $FeCl_3$ and $IrCl_3$ solutions and twice-distilled water were mixed, then TMAH was added as a precipitating agent (Table 1). The as-formed aqueous suspensions were vigorously shaken for about 10 min, then heated at 60 °C in plastic bottles (samples from HIR series) or at 160 °C in the autoclave (Parr general-purpose bomb, model 4744) comprising a Teflon vessel and a cup (samples from IrH series) [52]. After a proper heating time (Table 1) the precipitates were cooled to room temperature (mother liquor pH ≈13.5) and subsequently washed with twice-distilled water to remove the "neutral electrolyte". The ultraspeed *Sorvall* RC2-B centrifuge was used. Obtained pure and Ir-doped goethites were dried at 60 °C overnight. The pure goethite sample and selected Ir-doped goethites prepared at 60 °C were analyzed by X-ray powder diffraction (Fig. 1a). The XRD patterns of these samples showed only the presence of diffraction lines characteristic of goethite (JCPDS-ICDD PDF card No. 29-0713). The incorporation of Ir^{3+} ions into goethite led to the anisotropic narrowing of the diffraction lines and slight changes in their position due to changes in the unit cell dimensions [52]. In order to obtain hematites by the dehydroxylation of goethites, the prepared samples were heated in a laboratory furnace (air atmosphere) at 200 °C, then at 400 °C and finally at 600 °C for two hours at each temperature followed by slow cooling to room temperature. The TGA analysis of selected goethite precursors from room temperature to 600 °C showed an increase in the dehydroxylation temperature and a decrease in the overall weight loss with increasing iridium content (Fig. 1b). The obtained samples (pure and Ir-doped hematites) were characterized by X-ray powder diffraction (XRD), Mössbauer, FT-IR and UV–Vis–NIR spectroscopies, magnetic measurements (SQUID magnetometer), high-resolution scanning electron microscopy (FE-SEM) and energy dispersive X-ray spectroscopy (EDS).

2.2. Instrumentation

X-ray powder diffractometer APD 2000 (CuKα radiation, graphite monochromator, NaI-Tl detector) manufactured by *ItalStructures* (*G.N.R. s.r.l.*, Novara, Italy) was used.

Thermogravimetric analysis (TGA) of the studied goethite samples was carried out using a *TA Instruments* Q500 thermogravimetric analyzer in air atmosphere from room temperature to 600 °C at the heating rate of 10 °C/min.

^{57}Fe Mössbauer spectra were recorded at 20 °C (293 K) in the transmission mode using a standard *WissEl* (Starnberg, Germany) instrumental configuration. A $^{57}Co/Rh$ Mössbauer source was used. The velocity scale and all data refer to the metallic α-Fe absorber at 20 °C. A quantitative analysis of the recorded spectra was made using the *MossWinn* program.

Magnetic measurements were performed using a commercial SQUID magnetometer (*Quantum Design*, model MPMS-5). The powder samples were put into a small ampoule whose diamagnetic contribution was properly subtracted. The temperature dependence of magnetization was measured in an applied magnetic field of 100 Oe during the warming process in a broad temperature range around the expected Morin transition temperature (220–400 K).

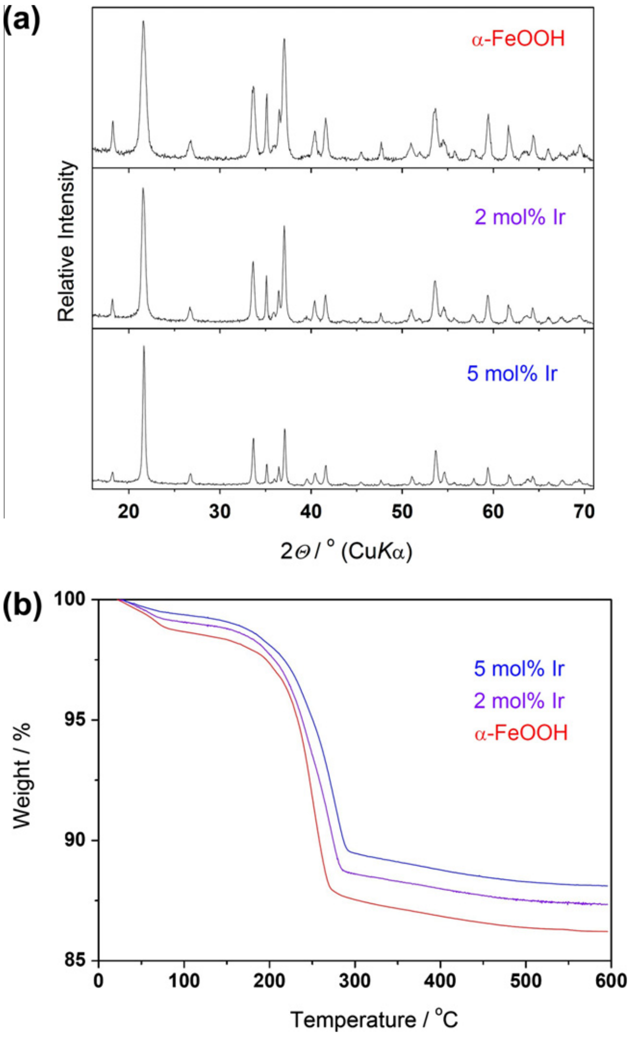

Fig. 1. XRD powder patterns (a) and TGA analysis (b) of pure and Ir-substituted goethite precursors synthesized at 60 °C. The nominal iridium content is marked.

Fourier transform infrared (FT-IR) spectra were recorded at RT using a *Perkin-Elmer* spectrometer (model 2000). The FT-IR spectrometer was connected to a PC with the installed IRDM (IR data manager) program to process the recorded spectra. The specimens were pressed into small discs using a spectroscopically pure KBr matrix.

Diffuse reflectance UV–Vis–NIR spectra were obtained at 20 °C using a *Shimadzu* UV–Vis–NIR spectrometer (model UV-3600) equipped with an integrated sphere. Barium sulfate was used as reference.

Table 1

Concentration conditions for sample preparation by hydrothermal treatment at 60 °C (HIR series) or 160 °C (IrH series) followed by heating the obtained powders in an oven at 200, 400 and 600 °C for 2 h at each temperature.

Sample	$[FeCl_3]$ (mol dm^{-3})	$[IrCl_3]$ (mol dm^{-3})	100·[Ir]/([Ir]+[Fe])	TMAH[a] (mol dm^{-3})	Aging time (hours)
HIR0	0.1	0	0	0.7	72
HIR001	0.1	1.00×10^{-5}	0.01	0.7	72
HIR03	0.1	1.00×10^{-5}	0.03	0.7	72
HIR01	0.1	1.00×10^{-4}	0.1	0.7	72
HIR02	0.1	2.00×10^{-4}	0.2	0.7	72
HIR05	0.1	5.03×10^{-4}	0.5	0.7	72
HIR1	0.1	1.01×10^{-3}	1	0.7	72
HIR2	0.1	2.04×10^{-3}	2	0.7	72
HIR5	0.1	5.27×10^{-3}	5	0.7	72
IrH0	0.1	0	0	0.7	2
IrH1	0.1	1.01×10^{-3}	1	0.7	2
IrH5	0.1	5.27×10^{-3}	5	0.7	2

[a] TMAH = tetramethylammonium hydroxide (25% w/w).

A thermal field emission scanning electron microscope (FE-SEM, model JSM-7000F, manufactured by *JEOL Ltd.*) was used. FE-SEM was linked to the EDS/INCA 350 (energy dispersive X-ray analyzer) manufactured by *Oxford Instruments Ltd.* The specimens were not coated with an electrically conductive surface layer.

3. Results and discussion

3.1. X-ray powder diffraction

The X-ray powder diffraction patterns of all prepared samples showed only the presence of diffraction lines typical of hematite (JCPDS-ICDD PDF card No. 33-0664). Diffraction patterns of samples HIR0, HIR1, HIR2 and HIR5 were analyzed in detail in order to elucidate the effect of incorporation of Ir^{3+} ions on the unit-cell parameters, crystallite size and strain in hematite.

Precise lattice parameters of the α-Fe_2O_3-type solid solutions were determined from the results of Le Bail refinements [55] of powder diffraction patterns (program GSAS [56] with a graphical user interface EXPGUI [57]). Silicon (Koch-Light Lab Ltd.) was used as an internal standard (space group $m3m$; $a = 5.43088$ Å; JCPDS-ICDD PDF card No. 27-1402). In all the cases the Rwp (weighted residual error) indexes of the refined patterns were less than 9%. Fig. 2 shows the observed and calculated powder patterns of the α-Fe_2O_3-type crystallization products with varying iridium

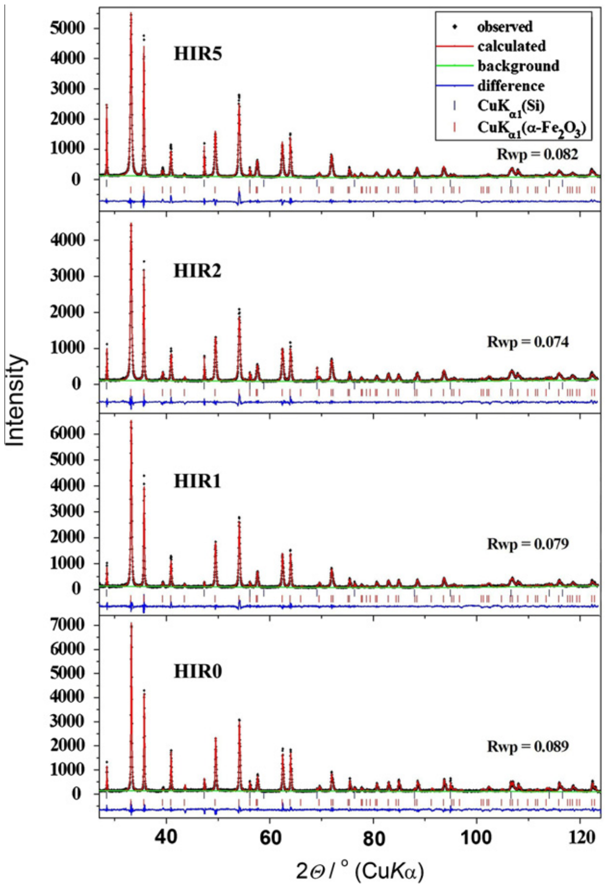

Fig. 2. The results of Le Bail refinements on powder diffraction patterns of crystallization products containing the α-Fe_2O_3-type solid solutions with a varying iridium content and silicon as an internal standard. The difference between the observed and calculated patterns is shown as a line in the lower field.

Table 2
Refined values of unit-cell parameters of the hematite-type phase with varying Ir content (given in mol%).

Sample	x_{Ir} (nominal)	x_{Ir} (by EDS)	Lattice parameters of hematite-type phase		R_{wp}
			a/nm	c/nm	
HIR0	0.0	0.0	0.50361(2)	1.37519(3)	0.089
HIR1	1.0	0.9	0.50379(2)	1.37529(3)	0.079
HIR2	2.0	1.6	0.50389(2)	1.37537(3)	0.074
HIR5	5.0	2.9	0.50406(2)	1.37556(3)	0.082

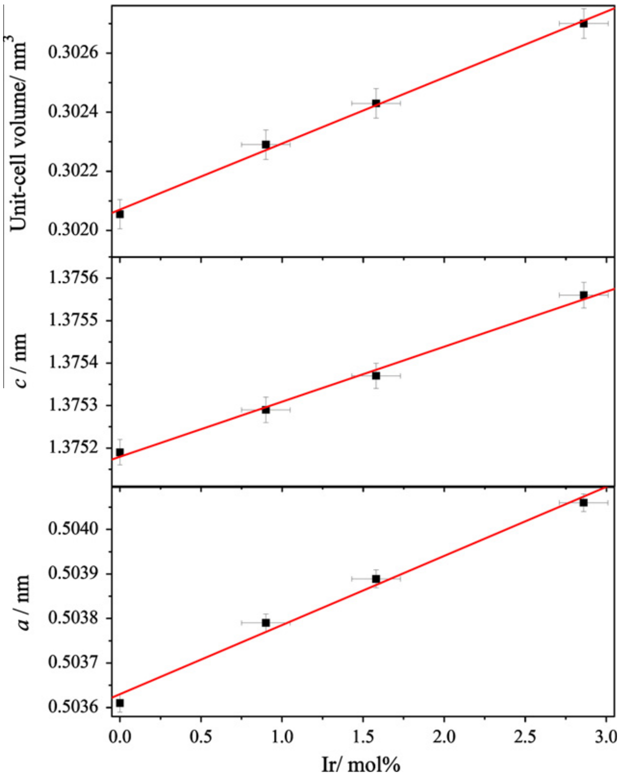

Fig. 3. Influence of the iridium content (determined by EDS) on unit-cell parameters a and c and the corresponding unit-cell volume of the α-Fe_2O_3-type solid solution.

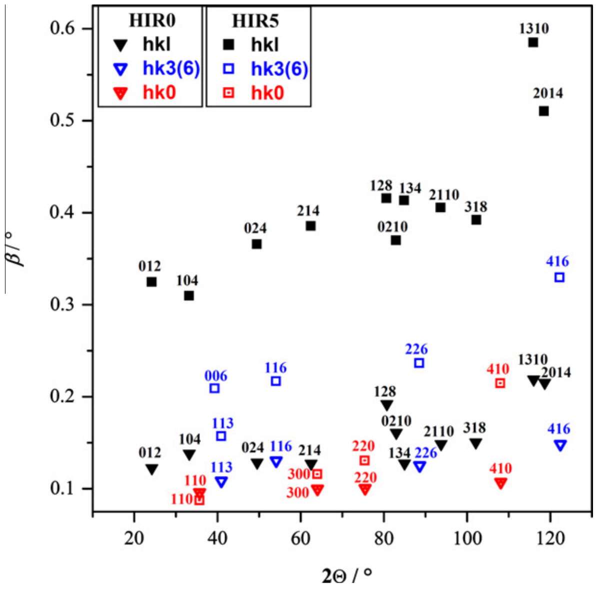

Fig. 4. 2θ dependence of the integral breadths of the physically broadened diffraction-line profiles (β) of samples HIR0 and HIR5.

Table 3
Values of volume-averaged domain size (D_v) and the root–mean–square strain (RMSS) of hematite-type samples (HIR0 and HIR5), estimated from reflections with the Miller index $l = 0$, 3 or 6 and $l = 2n$ ($n \neq 0$, 3) by using the double-Voigt method [59].

Sample	*x*Ir (nominal)	*x*Ir (by EDS)	*l* = 0		*l* = 3 or 6		*l* = 2*n* (*n* ≠ 0, *n* ≠ 3)	
			Dv	RMSS	*Dv*	RMSS	*Dv*	RMSS
HIR0	0.0	0.0	94 nm	–	76 nm	–	60 nm	–
HIR5	5.0	2.9	119 nm	3.6×10^{-4}	47 nm	–	27 nm	–

content. The refined unit-cell parameters of the α-Fe_2O_3-type product are listed in Table 2. The amounts of iridium incorporated into the hematite lattice were estimated from the results of EDS analysis (Table 2). Unlike the goethite-type solid solutions, which show asymmetric changes in the lattice parameters (parameter *b* increase and parameter *a* decrease with increasing iridium content) [52], the increase in the iridium content caused a linear increase in the parameters (*a* and *c*) and the corresponding unit-cell volume of the α-Fe_2O_3-type phase (Fig. 3). This slight increase in the unit-cell size is in line with a somewhat larger Ir^{3+} ions (ionic radius 0.68 Å) than Fe^{3+} ions (ionic radius 0.645 Å) [58].

The results of line broadening analysis indicate an anisotropic broadening of the hematite diffraction lines. In dependence on the values of the Miller index *l*, these lines can be separated into three groups: the narrowest diffraction lines with $l = 0$, somewhat broader diffraction lines with $l = 3$ or 6 and the broadest diffraction lines with $l = 2n$ ($n \neq 0$, 3). Anisotropic broadening significantly increases with the incorporation of iridium ions (Fig. 4). The volume-averaged domain size (D_v) and the root–mean–square strain (RMSS) of samples HIR0 and HIR5 were determined from the broadening of the diffraction lines according to the so-called 'double–Voigt' method [59] equivalent to the Warren–Averbach approach [60] (Table 3). This method, in which the Voigt functions were used to describe both the crystallite size and the microstrain broadening of the diffraction lines, was performed using the computer program BREADTH [61]. Physically broadened line profiles were obtained by applying the convolution-fitting approach (SHADOW program [62]) in which the instrumental profile (LaB_6 NIST SRM 660 powder diffraction lines) is convoluted with a refinable Voigt function to fit the observed diffraction line profiles. The obtained results (Table 3) indicate that, with an exception of the direction $l = 0$ of sample HIR5, the contribution of micro-strains to the line broadening is negligible.

3.2. ^{57}Fe Mössbauer spectroscopy

^{57}Fe Mössbauer spectra of pure hematite samples (HIR0 and IrH0) and Ir-doped hematite samples (with the given nominal iridium content) are shown in Figs. 5–7. The calculated Mössbauer parameters and phase identification are given in Table 4.

The room temperature Mössbauer spectrum of a pure, well-crystalline hematite is a sextet of quite narrow lines with a relatively large gap between them (large hyperfine magnetic splitting), and a closer 5th and 6th line than the 1st and 2nd (negative quadrupole splitting). The isomer shift of such hematite is usually reported at 0.37–0.38 mm s^{-1}, hyperfine magnetic field (HMF) at about 51.7–51.8 T and quadrupole splitting at −0.20 to −0.21 mm s^{-1} [1,63,64]. The spectra of samples HIR0 and IrH0 (Figs. 5 and 7) showed a good match with these characteristics, although the HMF values were slightly reduced due to the non-perfect crystallinity of hematite samples obtained by goethite dehydroxylation at 600 °C.

A specific feature of the magnetic structure of hematite is a change in the magnetic state at the Morin transition temperature ($T_M \approx 260$ K, for the samples with a very good crystallinity) [3,64–67]. Below the Morin transition temperature the magnetic spins of Fe^{3+} cations are oriented exactly antiparallel (an antiferromagnetic state, AFS) along a direction close to the hexagonal [0 0 1]

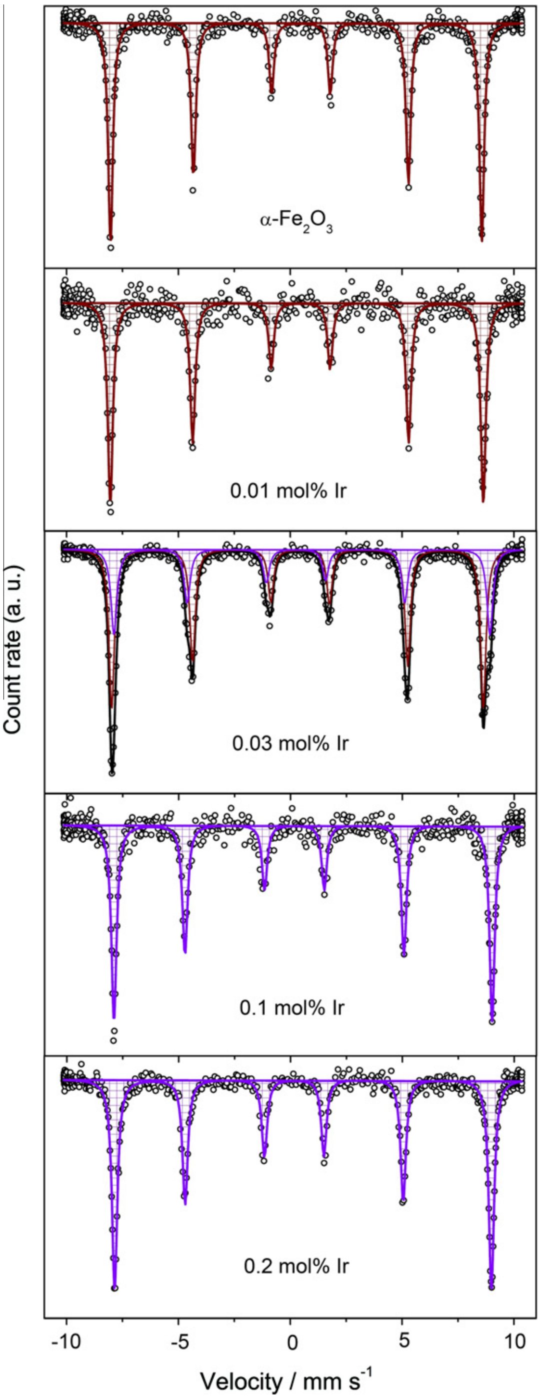

Fig. 5. ^{57}Fe Mössbauer spectra (recorded at 20 °C) of samples HIR0, HIR001, HIR003, HIR01 and HIR02. The nominal iridium content is marked.

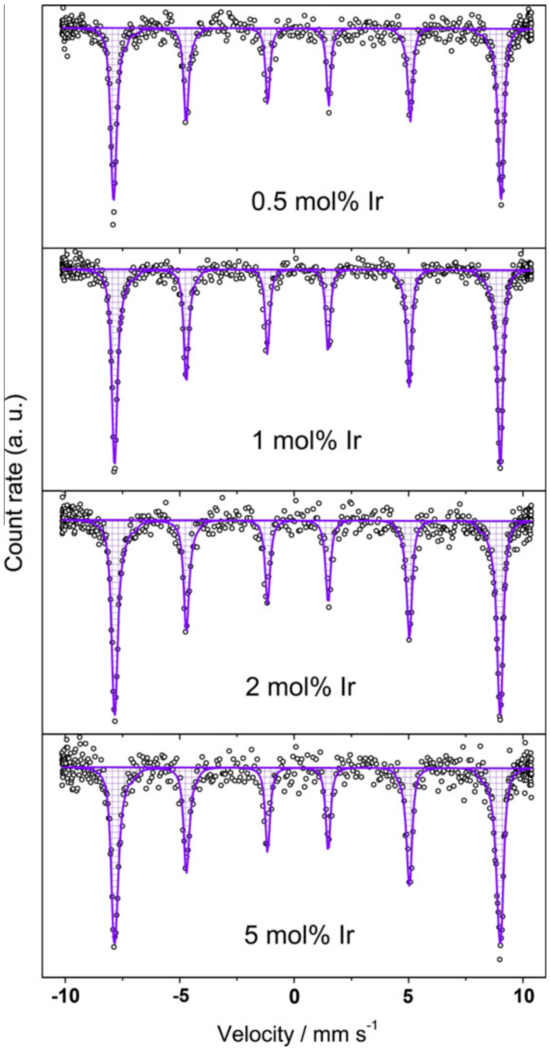

Fig. 6. ^{57}Fe Mössbauer spectra (recorded at 20 °C) of samples HIR05, HIR1, HIR2 and HIR5. The nominal iridium content is marked.

or rhombohedral [1 1 1] crystallographic direction. Above the Morin transition temperature and below the Curie temperature (T_C - ≈ 955 K) the magnetic spins of Fe^{3+} cations are oriented almost antiparallel, with a minor spin canting (a weakly ferromagnetic state, WFS), in the plane perpendicular to the hexagonal [0 0 1] or rhombohedral [1 1 1] direction.

The Morin transition temperature is sensitive to an external magnetic field and pressure, α-Fe_2O_3 particle size, crystal defects, lattice strain and incorporation of various metal cations into the α-Fe_2O_3 structure [3,64,66,69–71]. Most incorporated cations reduce or suppress this transition [3,11,15,33,68,72], whereas a few of them (Rh^{3+}, Ru^{3+} and Ir^{4+}), on the other hand, cause an increase in T_M [27,39,30,73]. This effect has been largely explained by an increase in the single-ion magnetic anisotropy component in hematite as a result of the incorporated strong anisotropy cations Rh^{3+}, Ru^{3+} or Ir^{4+}. In our previous work [52] the Mössbauer spectroscopy analysis confirmed the antiferromagnetic order (characteristic of hematite at temperatures below T_M) in the Ir^{3+}-doped hematite at 293 K and thus clearly demonstrated the effect of the incorporation of this cation into hematite on the increase in the Morin transition temperature.

The Mössbauer spectrum of hematite nominally doped with 0.01% iridium (Fig. 5) showed no change in magnetic state (WFS) relative to pure hematite, with only slight changes in Mössbauer parameters (Table 4). However, the spectrum of the sample with 0.03% iridium clearly showed the presence of two magnetic states in that sample. The values of quadrupole splitting obtained by fitting are significantly shifted from the expected values for hematite in both AFS and WFS. Most likely this is the consequence of a deflected magnetic moment direction relative to its direction in AFS ([0 0 1] direction) and WFS (perpendicular to [0 0 1] direction), respectively [74,75]. Mössbauer spectra of samples doped with 0.1% iridium or more showed the presence of an exclusively magnetic sextet characteristic of hematite in AFS (Figs. 5–7). The value of quadrupole splitting increased with an increase in the iridium concentration in hematite (Table 4). This observation can be explained by small changes in the magnetic moment direction or by a slight distortion in the hematite structure through the incorporation of iridium ions [27,75]. A slight broadening of Mössbauer lines to a lower hyperfine magnetic field with an increase in the iridium ion content was also observed (Table 4). It can be explained by the impact of incorporated iridium ions and the reduction in crystallinity (as observed by XRD, Section 3.1).

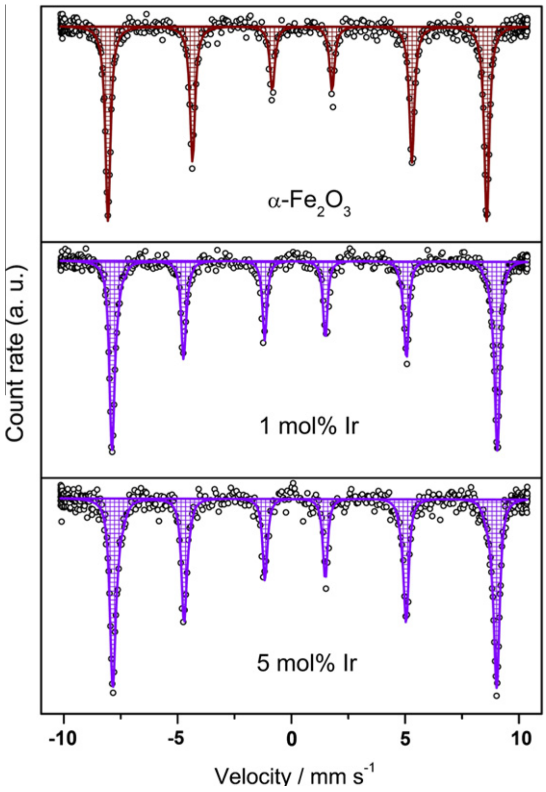

Fig. 7. ^{57}Fe Mössbauer spectra (recorded at 20 °C) of samples IrH0, IrH1 and IrH5. The nominal iridium content is marked.

The relative areas of the lines in the Mössbauer sextet are dependent on the angle between the respective γ-rays direction and the effective magnetic flux density [67,76]. If the magnetic moments of iron atoms in a sample are pointed in random directions relative to the incident γ-rays then the relative line areas (intensities) of the resultant sextet will average out to ratio of 3:2:1:1:2:3. If there is some preferred orientation of these magnetic moments, the relative areas of the 2nd and 5th line will deviate from 2. If the magnetic moments prefer to orientate at higher angles relative to the incident γ-rays, then the relative areas of the 2nd and 5th line will be above 2. This is the case in the spectra of WF hematite samples (HIR0, IrH0 and HIR001) (Table 4) where hematite particles (obtained by the dehydroxylation of goethite particles) are somewhat preferentially oriented, with the [0 0 1] direction tending to be parallel to the incident γ-rays, i.e. with the magnetic moments

Table 4
^{57}Fe Mössbauer parameters at 20 °C calculated for synthesized samples and phase identification.

Sample	Spectral line	RLA[b] 2nd; 5th	δ (mm s^{-1})	2ε (mm s^{-1})	Bhf (T)	Γ (mm s^{-1})	Area (%)	Phase
HIR0	M	2.1; 2.2	0.37	−0.21	51.5	0.26	100	WF α-Fe_2O_3
HIR001	M	2.1; 2.2	0.38	−0.17	51.7	0.28	100	WF α-Fe_2O_3
HIR003	M	2.1; 2.2	0.37	−0.12	51.6	0.30	63.5	WF α-Fe_2O_3
	M	1.9;1.9	0.38	0.27	52.2	0.33	36.5	AF α-Fe_2O_3
HIR01	M	1.7; 1.7	0.37	0.39	52.4	0.28	100	AF α-Fe_2O_3
HIR02	M	1.4; 1.4	0.37	0.40	52.3	0.29	100	AF α-Fe_2O_3
HIR05	M	1.5; 1.6	0.38	0.40	52.2 (52.5)[a]	0.22	100	AF α-Fe_2O_3
HIR1	M	1.5; 1.6	0.37	0.42	51.9 (52.3)[a]	0.22	100	AF α-Fe_2O_3
HIR2	M	2.1; 2.2	0.37	0.42	51.8 (52.3)[a]	0.24	100	AF α-Fe_2O_3
HIR5	M	1.6; 1.6	0.37	0.42	51.8 (52.3)[a]	0.23	100	AF α-Fe_2O_3
IrH0	M	2.1; 2.2	0.37	−0.21	51.6	0.27	100	WF α-Fe_2O_3
IrH1	M	1.4; 1.4	0.37	0.42	52.2 (52.5)[a]	0.22	100	AF α-Fe_2O_3
IrH5	M	1.7; 1.7	0.38	0.42	51.8 (52.3)[a]	0.22	100	AF α-Fe_2O_3

Errors: $\delta = \pm 0.01$ mm s^{-1}, $2\varepsilon = \pm 0.01$ mm s^{-1}, Bhf = ± 0.2 T, $\Gamma = \pm 0.01$ mm s^{-1}.
Isomer shift is given relative to α-Fe.

[a] Average Bhf (first value) and the most probable Bhf (in parenthesis).

[b] Relative line area (RLA) of second and fifth line in a magnetically split sextet (RLA is 2 in a randomly oriented sample with line intensity ratio 3:2:1:1:2:3).

(which are perpendicular to [001]) being on the average at higher angles relative to the incident γ-rays. Such increase in the relative areas of 2nd and 5th line in Mössbauer spectra due to the preferential orientation of the magnetic moments was also observed for elongated goethite particles [54]. However, in the case of Mössbauer spectra of AF hematite samples the magnetic moments are oriented in the [001] direction. Owing to the lath-shaped hematite particles (Figs. 12 and 13) the lower angles between the magnetic moments of iron atoms and the incident γ-rays are preferred, i.e., the relative areas of the 2nd and 5th line in Mössbauer spectra are below 2 (Figs. 5–7 and Table 4).

3.3. Magnetic measurements

The temperature dependence of magnetization for selected samples (pure hematite and Ir-doped hematites with the lowest iridium concentrations) is shown in Fig. 8. Generally, the increased concentration of iridium dopant led to an increase in the Morin transition temperature (T_M) and a decrease in WFS magnetization. The Morin transition temperature was determined from the inflection point of the magnetization-temperature curve at 256, 293, 309 and 326 K for samples HIR0, HIR001, HIR003 and HIR01, respectively. These results deviate to a certain extent from Mössbauer measurements which revealed that sample HIR001 is completely in the WFS at 293 K and sample HIR03 is in both the WFS and AFS at the same temperature (Fig. 5 and Table 4). This deviation can be explained by the fact that the transition from the AFS to WFS measured by warming the sample occurs at a higher temperature than the transition from the WFS to the AFS measured by cooling the sample [71,77]. The magnetic state can thus be different for the same sample at the same temperature depending on the sample's temperature history. The Mössbauer measurements were conducted at 20 °C on the samples cooled to that temperature from higher temperatures and, contrariwise, the SQUID magnetic measurements were conducted by warming the samples from lower to higher temperatures.

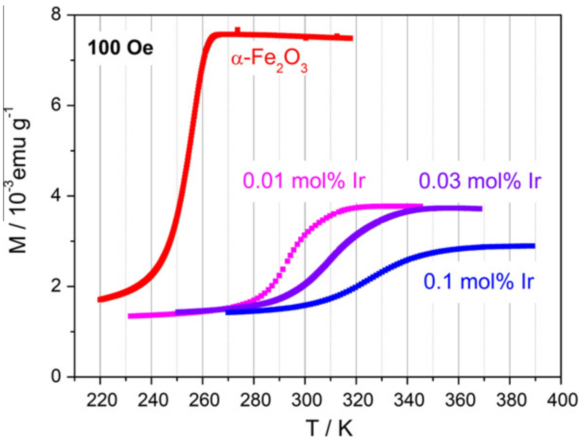

Fig. 8. Temperature dependence of magnetization measured in an applied magnetic field of 100 Oe during a warming process for samples HIR0, HIR001, HIR003 and HIR01. The nominal iridium content is marked.

3.4. FT-IR spectroscopy

The dominant features in the infrared spectrum of hematite are strong and broad absorption bands in the wavenumber range from about 700 to 200 cm^{-1} which are caused by crystal lattice vibrations. The crystal structure of hematite allows the existence of six IR active modes, two of which are A_{2u} modes, with polarization parallel to the crystallographic c-axis, and four are E_u modes, with polarization perpendicular to the c-axis [78,79]. Appearance of the infrared spectrum of hematite is remarkably dependent on the microstructural properties of the recorded sample. It is a well known fact that the positions of infrared bands in the IR spectra of various hematites are related to the particle shape and size due to the polarization charge induced at the particle surface by an external electromagnetic field [79–83]. Gradual shifts in the position of hematite infrared bands have also been observed in the spectra of hematite samples with Fe^{3+} cations substituted by some other metal cations [5,8,11,84,85].

The characteristic part of the FT-IR spectra of pure and Ir-doped hematite samples from HIR and IrH series is shown in Figs. 9 and 10, respectively. The positions of infrared bands in undoped samples (HIR0 and IrH0) are labeled by dotted vertical lines. The positions of infrared bands are listed in Table 5. The spectra of pure hematite samples (HIR0 and IrH0) are almost identical and very similar to the IR spectrum of sintered hematite particles without a well-defined shape obtained by heating goethite [79,86]. An increase in the content of Ir^{3+} ions in hematite led to a gradual shift of E_u mode vibration bands to lower wavenumbers and that of A_{2u} mode vibration bands to higher wavenumbers. This kind of shifts in infrared band position was observed in hematite samples with an increased particle length in a direction perpendicular to the c-axis in comparison with particle length in a direction parallel to the c-axis (lath-like and disc-like hematite particles) [79,82,83]. The presence of heavier Ir^{3+} ions embedded in the crystal structure

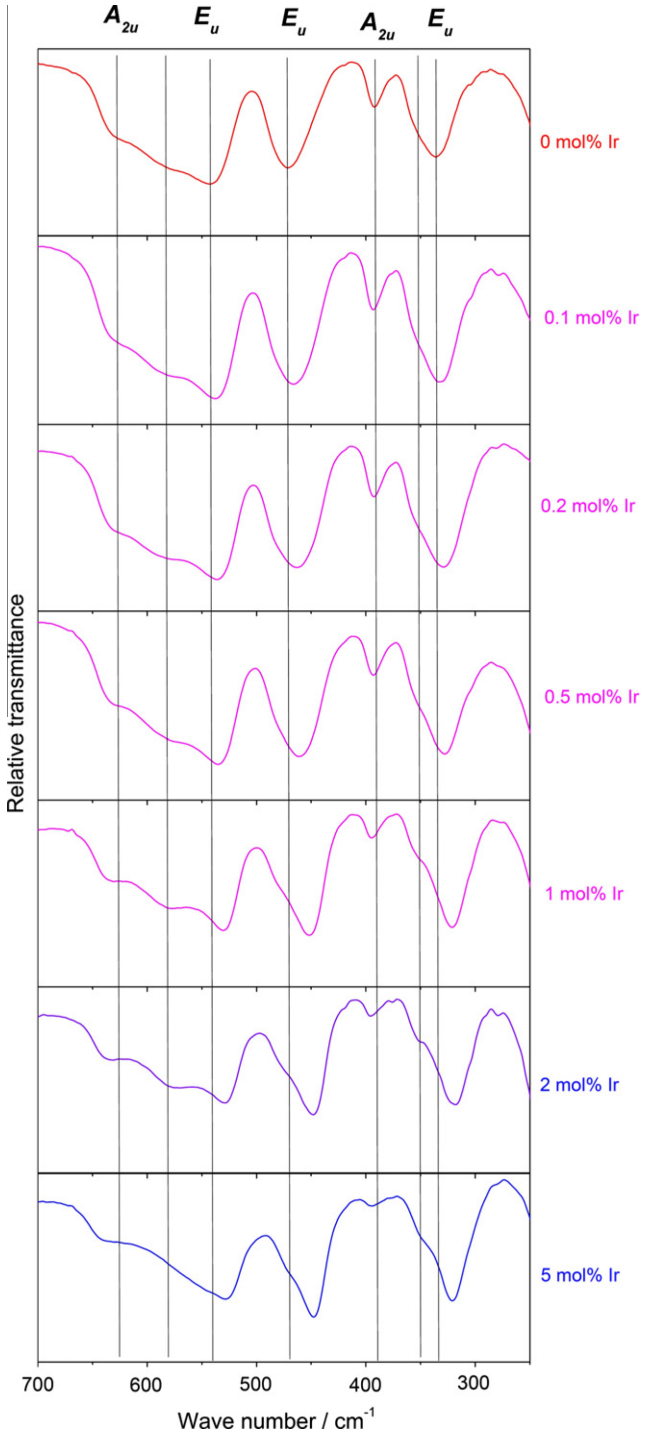

Fig. 9. The FT-IR spectra of HIR series samples. The nominal iridium content is marked. Positions of infrared bands in the HIR0 sample spectrum are marked by vertical lines.

of hematite is likely to contribute to such shifts. The spectra of samples containing the highest levels of iridium dopant are similar to the IR spectra of lath-like hematite particles obtained by heating goethite at temperatures lower than 600 °C [79,86,87], and also to the IR spectra of plate-like hematite particles obtained by crystal growth in a solution [82,83,88]. Shoulders at about 580 and 350 cm^{-1} most likely come from the absorption of infrared radiation by irregular and near spherical hematite particles (both A_{2u} and E_u modes at 580 cm^{-1} and E_u mode at 350 cm^{-1}) [80,81,89,90] formed by sintering the lath-like hematite particles which, in turn, were obtained by the dehydroxylation of goethite particles (Figs. 12 and 13, Section 3.6).

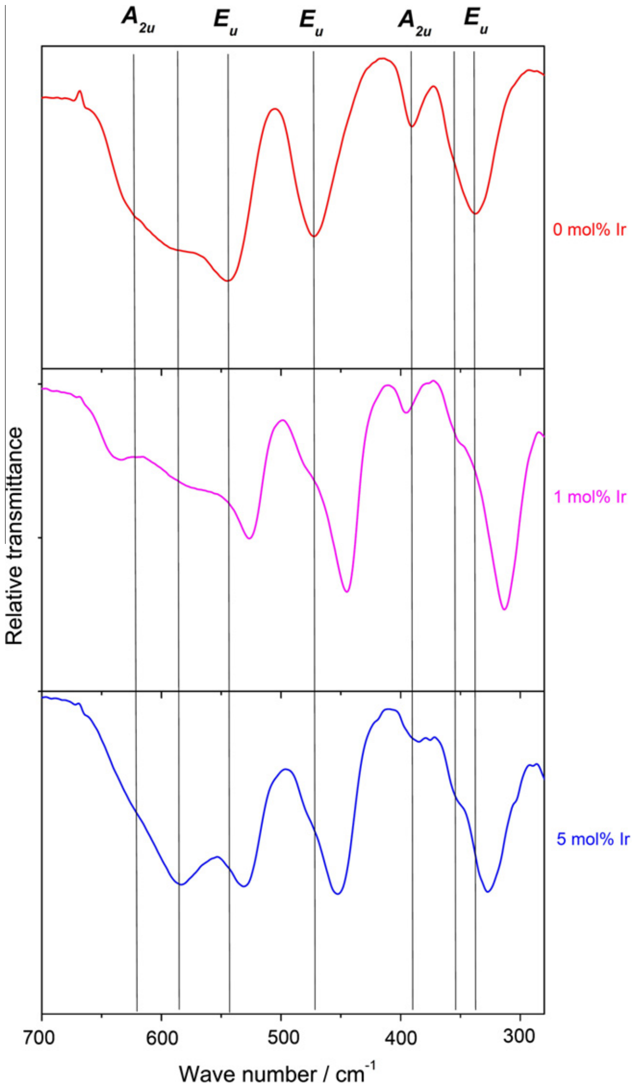

Fig. 10. The FT-IR spectra of IrH series samples. The nominal iridium content is marked. Positions of infrared bands in the IrH0 sample spectrum are marked by vertical lines.

3.5. Diffuse reflectance UV–Vis–NIR spectroscopy

The iron oxide spectra in near infrared, visible and ultraviolet spectral regions are caused by transitions between the electronic states. Three types of such transitions are generally accepted [1,91,92]: (a) the Fe^{3+} ligand field transitions, (b) the ligand (oxygen) to metal (iron) charge-transfer transitions and (c) the transitions by simultaneous excitation of magnetically-coupled Fe^{3+} cations. The energies of some of these transitions are located in the visible part of the spectrum (~380–750 nm) and, consequently, the positions and intensities of corresponding bands are responsible for various colors of iron oxides. Color variations between pure and Ir-doped hematites indicate differences in the visible spectra of these samples.

Diffuse reflectance UV–Vis–NIR spectra of selected samples in the range from 300 to 1500 nm are shown in Fig. 11. The spectrum of sample HIR0 (pure α-Fe_2O_3) shows a generally low absorption in the near infrared region (800–1500 nm) with a weak and broad

Table 5
Band positions in the FT-IR spectra of pure and Ir-doped hematite samples.

Sample	Wave number of IR active modes (cm^{-1})				
	A_{2u}	E_u	E_u	A_{2u}	E_u
H60	625	543	472	392	336
HIR01	627	538	466	393	333
HIR02	628	536	463	393	329
HIR03	630	535	461	395	328
HIR1	632	531	452	396	321
HIR2	635	529	448	396	318
HIR3	640	543	448	394	321
H160	620	545	472	391	338
IrH1	633	527	445	395	313
IrH5	625	531	453	385	327

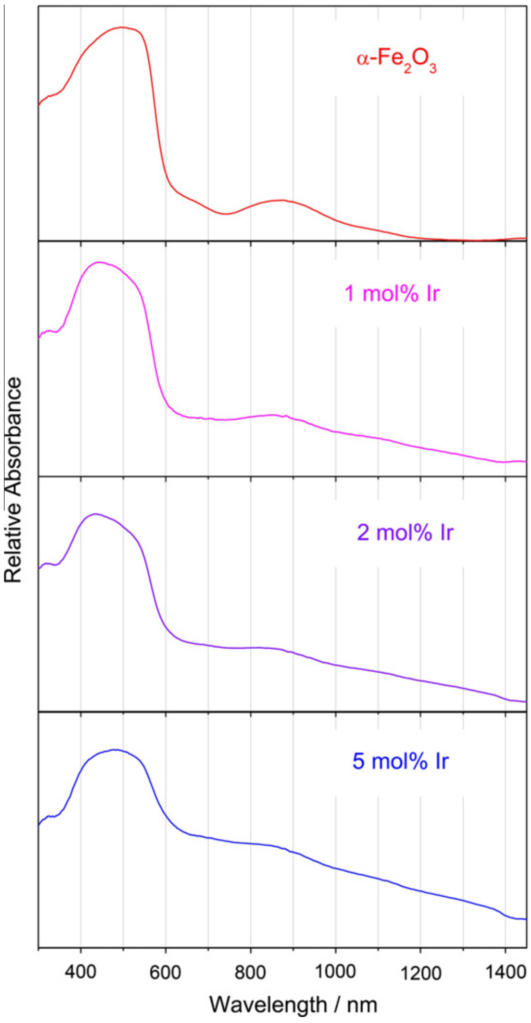

Fig. 11. The UV–Vis–NIR spectra of samples HIR0, HIR1, HIR2 and HIR5. The nominal iridium content is marked.

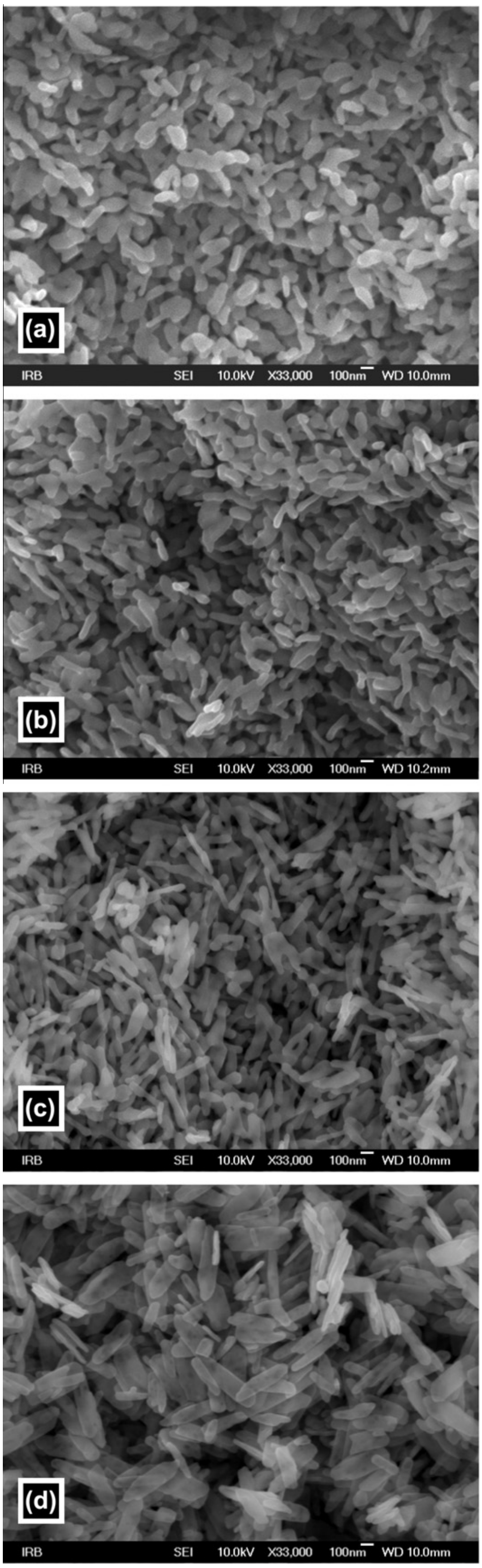

Fig. 12. FE-SEM images of samples HIR0 (a), HIR01 (b), HIR1 (c), and HIR5 (d).

absorption band centered at 870 nm as the only feature. This band is assigned [92] to $^6A_1 \rightarrow {}^4T_1$ ligand field transition which corresponds to electron excitation from the Fe^{3+} ground state (in which all spins of three electrons in the t_{2g} 3d-orbitals and two electrons in the e_g 3d-orbitals are in the same direction) to the first excited state (in which one electron from the e_g level comes to the t_{2g} level with the opposite spin direction). In the visible part of the spectrum the first feature is a weak shoulder at about 650 nm which is assigned to $^6A_1 \rightarrow {}^4T_2$ ligand field transition [92]. A steep increase in absorption (absorption edge) takes place between about 600 to 540 nm, and an inflection point of this curve (~570 nm) corresponds to the energy of a band gap (~2.2 eV) in α-Fe$_2$O$_3$ [1,93]. Strong absorption in the region from about 380 to 570 nm is a

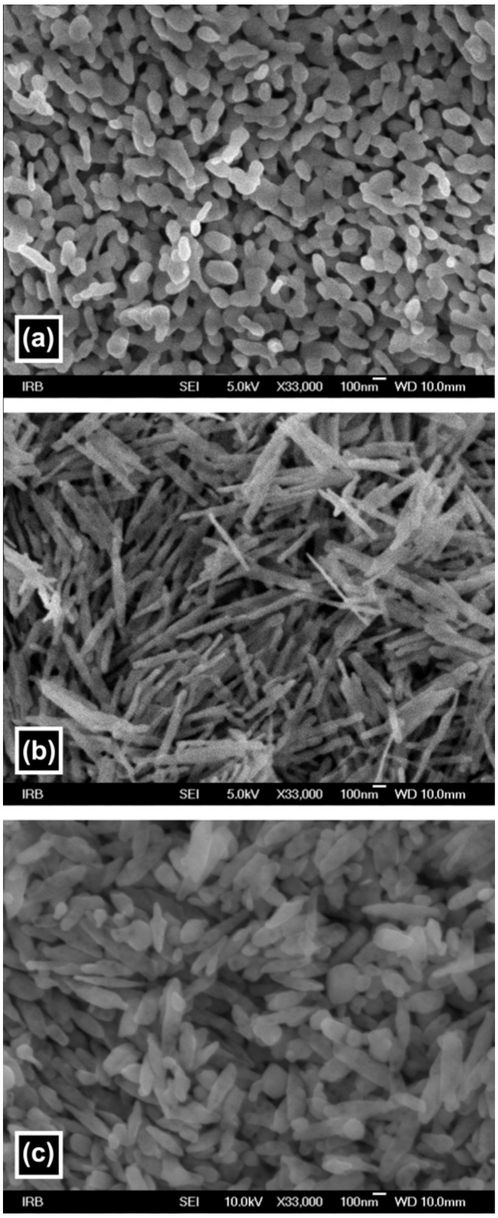

Fig. 13. FE-SEM images of samples IrH0 (a), IrH1 (b), and IrH5 (c).

result of an overlap of the bands caused by two different transitions [92]: electron pair transition $^6A_1 + {}^6A_1 \rightarrow {}^4T_1 + {}^4T_1$ (resulting from magnetic coupling of adjacent Fe^{3+} cations) at about 530 nm and "spin-flip" transition $^6A_1 \rightarrow {}^4E,{}^4A_1$ (change in the spin orientation of one electron in relation to the ground state configuration) at about 440 nm. Systematic investigations performed on various hematite samples showed that the positions and intensities of these electron transition bands depend on the size and shape of particles and their crystallinity [94–98], as well as the doping of metal cations [8,18,23,85].

The spectra of the Ir-doped hematite samples (Fig. 11) showed significant differences in comparison with the spectrum of a pure hematite sample. Radiation absorption in the red and near infrared regions by the Ir-doped hematites was significantly increased with an increase in iridium dopant concentration. At the same time, the inflection point of the absorption edge (caused by the electron pair transition $^6A_1 + {}^6A_1 \rightarrow {}^4T_1 + {}^4T_1$) was shifted from 574 nm (2.16 eV) in the spectrum of pure hematite to 568 nm (2.19 eV), 562 nm (2.21 eV) and 570 nm (2.18 eV) in the spectra of 1, 2 and 5 mol% Ir-doped hematite samples, respectively. These spectral differences can be ascribed to the simultaneous influence of changes in particle shape (Fig. 12, Section 3.5) and crystallite size (Section 3.1), as well as contribution due to the incorporation of Ir^{3+} ions into the hematite structure. Wang et al. [96] investigated the influence of the size and shape of hematite particles on the appearance of corresponding UV–Vis–NIR diffuse reflectance spectra. They observed higher absorbance (lower reflectance) in the red and near infrared regions of platelet hematite particles in comparison with polyhedral hematite particles. The optical gap was observed at 560 nm (2.22 eV) for polyhedral hematite particles, and at 580 nm (2.14 eV) for platelet hematite particles. Lu et al. [95] observed a shift of the electron pair transition $^6A_1 + {}^6A_1 \rightarrow {}^4T_1 + {}^4T_1$ to higher energies (lower wavelengths) with a reduction in the crystallite size of hematite samples. Based on these data and our analysis of UV–Vis–NIR diffuse reflectance spectra of Ir-doped hematite samples, we would suggest that Ir-doping together with the reduction in crystallite size was responsible for the shift of the absorption edge to higher energies (lower wavelengths). At the same time, the change in particle shape to lath-like hematite particles (sample with 5 mol% Ir) contributes to a shift of the absorption edge to lower energies (higher wavelengths).

3.6. FE-SEM

The FE-SEM images of selected samples from HIR series and all three samples from IrH series are shown in Figs. 12 and 13, respectively. Undoped hematite samples HIR0 (Fig. 12a) and IrH0 (Fig. 13a) consisted of somewhat sintered, fairly uniform hematite particles of a mainly ellipsoidal shape. The particles in sample IrH0 were slightly larger in comparison with sample HIR0 particles. The size and shape of hematite particles were defined by the size and shape of goethite precursor lath-like particles. A gradual elongation of hematite particles with an increase in iridium concentration is well visible, which is in line with the observed gradual shifts in the infrared absorption bands (Section 3.4). The shape of thin (clearly transparent) lath-like hematite particles of the sample containing the highest iridium concentration (HIR5, Fig. 12d) is in line with what is expected from the infrared spectrum (the highest wavenumber of E_u mode bands and the lowest wavenumber of A_{2u} mode bands among the IR spectra of all samples). Holes in hematite particles formed by the coalescence of the dehydroxylation pores are well visible in the image of this sample. The FE-SEM image of sample IrH1 (Fig. 13b) showed the highest elongation of hematite particles (400–600 nm in length) due to highly elongated particles of the Ir-doped goethite precursor [52]. The mixture of lath-like and nearly spherical Ir-doped hematite particles is visible in the FE-SEM image of sample IrH5 (Fig. 13c). This sample was obtained by heating the precursor sample consisting of lath-like Ir-doped goethite particles and nearly spherical Ir-doped hematite [52]. A strong band at 580 cm^{-1} corresponding to spherical hematite particles [79,80,89,90] is well visible in the infrared spectrum (Fig. 10) of the sample.

4. Conclusions

- A series of hematites doped with up to 5 mol% of Ir^{3+} ions was prepared by heating the hydrothermally prepared Ir-doped goethites.
- Doping by iridium ions caused an increase in the temperature of goethite dehydroxylation and suppressed the disappearance of holes in the formed hematite particles and their sintering.
- Incorporation of iridium ions into the hematite structure led to an increase in unit cell dimensions and a decrease in crystallite size.

- The Morin transition temperature increased whilst the magnetization of weakly ferromagnetic state decreased with an increase in Ir-doping.
- The presence of iridium ions brought about changes in the size and shape of the formed hematite particles.
- Infrared and UV–Vis properties of hematite samples were significantly affected by the incorporated iridium ions and by changes in the size, shape and crystallinity of hematite particles.

References

[1] R.M. Cornell, U. Schwertmann, The Iron Oxides, Structure, Properties, Reactions, Occurrence and Uses, second ed., Wiley-VCH, Weinheim, 2003.

[2] R.L. Blake, R.E. Hessevick, T. Zoltai, L.W. Finger, Am. Mineral. 51 (1966) 123–129.

[3] A.H. Morrish, Canted Antiferromagnetism: Hematite, World Scientific Publishing Co., Singapore, 1994.

[4] U. Schwertmann, R.W. Fitzpatrick, R.M. Taylor, D.G. Lewis, Clays Clay Miner. 27 (1979) 105–112.

[5] V. Barron, J.L. Rendon, J. Torrent, C.J. Serna, Clays Clay Miner. 32 (1984) 475–479.

[6] S. Musić, S. Popović, M. Ristić, J. Mater. Sci. 24 (1989) 2722–2726.

[7] M. Ristić, S. Popović, M. Tonković, S. Musić, J. Mater. Sci. 26 (1991) 4225–4233.

[8] S. Musić, M. Lenglet, S. Popović, B. Hannoyer, I. Czakó-Nagy, M. Ristić, D. Balzar, F. Gashi, J. Mater. Sci. 31 (1996) 4067–4076.

[9] F.J. Berry, C. Greaves, J. McManus, M. Mortimer, G. Oates, J. Solid State Chem. 130 (1997) 272–276.

[10] F.J. Berry, A. Bohorquez, C. Greaves, J. McManus, E.A. Moore, M. Mortimer, J. Solid State Chem. 140 (1998) 428–430.

[11] G.M. da Costa, E. Van San, E. De Grave, R.E. Vandenberghe, V. Barrón, L. Datas, Phys. Chem. Miner. 29 (2002) 122–131.

[12] M. Sorescu, L. Diamandescu, D. Tarabasanu-Mihaila, J. Phys. Chem. Solids 65 (2004) 1719–1725.

[13] S. Krehula, S. Musić, J. Mol. Struct. 834–836 (2007) 154–161.

[14] S. Krehula, S. Musić, J. Alloys Compd. 431 (2007) 56–64.

[15] E.E. Sileo, D.P. Daroca, Barrero, Larralde, Giberti, Saragovi, Chem. Geol. 238 (2007) 84–93.

[16] M. Ristić, S. Popović, S. Musić, Croat. Chem. Acta 82 (2009) 397–404.

[17] M. Sorescu, L. Diamandescu, A. Tomescu, S. Krupa, Physica B 404 (2009) 2159–2165.

[18] M. Gaudon, N. Pailhé, J. Majimel, A. Wattiaux, J. Abel, A. Demourgues, J. Solid State Chem. 183 (2010) 2101–2109.

[19] A. Gajović, A.M.T. Silva, R.A. Segundo, S. Šturm, B. Jančar, M. Čeh, Appl. Catal. B-Environ. 103 (2011) 351–361.

[20] M. Sorescu, T. Xu, L. Diamandescu, D. Hileman, Hyperfine Interact. 199 (2011) 365–386.

[21] P. Liao, M.C. Toroker, E.A. Carter, Nano Lett. 11 (2011) 1775–1781.

[22] J.-M. Tulliani, C. Baroni, C. Lopez, L. Dessemond, J. Eur. Ceram. Soc. 31 (2011) 2357–2364.

[23] J. Liu, C. Liang, H. Zhang, Z. Tian, S. Zhang, J. Phys. Chem. C 116 (2012) 4986–4992.

[24] V. Barron, J. Torrent, Clays Clay Miner. 32 (1984) 157–158.

[25] G. Buxbaum, G. Pfaff, Industrial Inorganic Pigments, Wiley-VCH, 2005.

[26] T.I. Bhuiyan, M. Nakanishi, Y. Kusano, T. Fujii, J. Takada, Y. Ikeda, Mater. Lett. 61 (2007) 3774–3777.

[27] J.M.D. Coey, G.A. Sawatzky, J. Phys. C: Solid State Phys. 4 (1971) 2386–2407.

[28] E. De Grave, L.H. Bowen, S.B. Weed, J. Magn. Magn. Mater. 27 (1982) 98–108.

[29] J.Z. Liu, C.L. Fan, Phys. Lett. 105A (1984) 80–82.

[30] J.Z. Liu, J. Magn. Magn. Mater. 54–57 (1986) 901–902.

[31] M.A. Wells, R.W. Fitzpatrick, R.J. Gilkes, J. Dobson, Geophys. J. Int. 138 (1999) 571–580.

[32] F.J. Berry, C. Greaves, Ö. Helgason, J. McManus, H.M. Palmer, R.T. Williams, J. Solid State Chem. 151 (2000) 157–162.

[33] I. Ayub, F.J. Berry, R.L. Bilsborrow, Ö. Helgason, R.C. Mercader, E.A. Moore, S.J. Stewart, P.G. Wynn, J. Solid State Chem. 156 (2001) 408–414.

[34] K. Urasaki, N. Tanimoto, T. Hayashi, Y. Sekine, E. Kikuchi, M. Matsukata, Appl. Catal. A 288 (2005) 143–148.

[35] F.J. Pérez-Alonso, M.L. Granados, M. Ojeda, T. Herranz, S. Rojas, P. Terreros, J.L.G. Fierro, M. Gracia, J.R. Gancedo, J. Phys. Chem. B 110 (2006) 23870–23880.

[36] J.Z. Jiang, R. Lin, W. Lin, K. Nielsen, S. Mørup, K. Dam-Johansen, R. Clasen, J. Phys. D: Appl. Phys. 30 (1997) 1459–1467.

[37] O.K. Tan, W. Cao, Y. Hu, W. Zhu, Ceram. Int. 30 (2004) 1127–1133.

[38] Y. Wang, F. Kong, B. Zhu, S. Wang, S. Wu, W. Huang, Mater. Sci. Eng. B 140 (2007) 98–102.

[39] M.A. Lukowski, S. Jin, J. Phys. Chem. C 115 (2011) 12388–12395.

[40] K. Sivula, F. Le Formal, M. Grätzel, ChemSusChem 4 (2011) 432–449.

[41] A. Kay, I. Cesar, M. Grätzel, J. Am. Chem. Soc. 128 (2006) 15714–15721.

[42] I. Cesar, A. Kay, J.A. Gonzalez Martinez, M. Grätzel, J. Am. Chem. Soc. 128 (2006) 4582–4583.

[43] J.A. Glasscock, P.R.F. Barnes, I.C. Plumb, N. Savvides, J. Phys. Chem. C 111 (2007) 16477–16488.

[44] I. Cesar, K. Sivula, A. Kay, R. Zboril, M. Grätzel, J. Phys. Chem. C 113 (2009) 772–782.

[45] Y. Ling, G. Wang, D.A. Wheeler, J.Z. Zhang, Y. Li, Nano Lett. 11 (2011) 2119–2125.

[46] A. Bak, W. Choi, H. Park, Appl. Catal. B-Environ. 110 (2011) 207–215.

[47] A. Punnoose, T. Phanthavady, M.S. Seehra, N. Shah, G.P. Huffman, Phys. Rev. B 69 (2004) 054425.

[48] F.J. Berry, X. Changhai, S. Jobson, J. Chem. Soc., Faraday Trans. 86 (1990) 165–169.

[49] F.J. Berry, S. Jobson, Hyperfine Interact. 69 (1991) 775–778.

[50] W. Zhang, Y. Huang, J. Wang, K. Liu, X. Wang, A. Wang, T. Zhang, Int. J. Hydrogen Energy 35 (2010) 3065–3071.

[51] S.D. Tilley, M. Cornuz, K. Sivula, M. Grätzel, Angew. Chem. Int. Ed. 49 (2010) 6405–6408.

[52] S. Krehula, S. Musić, J. Alloys Compd. 516 (2012) 207–216.

[53] S. Krehula, S. Popović, S. Musić, Mater. Lett. 54 (2002) 108–113.

[54] S. Krehula, S. Musić, J. Cryst. Growth 310 (2008) 513–520.

[55] A. Le Bail, H. Duroy, J.L. Fourquet, Mater. Res. Bull. 23 (1988) 447–452.

[56] A.C. Larson, R.B. Von Dreele, General Structure Analysis System GSAS, Los Alamos National Laboratory Report, 2001.

[57] B.H. Toby, J. Appl. Cryst. 34 (2001) 210–213.

[58] R.D. Shannon, Acta Cryst. A32 (1976) 751–767.

[59] D. Balzar, H. Ledbetter, J. Appl. Cryst. 26 (1993) 97–103.

[60] B.E. Warren, X-ray Diffraction, Addison Wesley, Reading, MA, 1969.

[61] D. Balzar, BREADTH – a program for analyzing diffraction line broadening, J. Appl. Cryst. 28 (1995) 244–245.

[62] S.A. Howard, R.L. Snyder, Adv. X-ray Anal. 26 (1983) 73–81.

[63] E. Murad, U. Schwertmann, Clays Clay Miner. 34 (1986) 1–6.

[64] E. Murad, J.H. Johnston, Iron Oxides and Oxyhydroxides, in: G.J. Long (Ed.), Mössbauer Spectroscopy Applied to Inorganic Chemistry, vol. 2, Plenum Publishing Corporation, New York, 1987, pp. 507–582.

[65] F.J. Morin, Phys. Rev. 78 (1950) 819–820.

[66] W. Kündig, H. Bömmel, Phys. Rev. 142 (1966) 327–333.

[67] E. De Grave, G.M. da Costa, L.H. Bowen, C.A. Barrero, R.E. Vandenberghe, Hyperfine Interact. 117 (1998) 245–270.

[68] P.J. Besser, A.H. Morrish, C.V. Searle, Phys. Rev. 153 (1967) 632–640.

[69] D. Schroeer, R.C. Nininger, Phys. Rev. Lett. 19 (1967) 632–634.

[70] R.D. Zysler, D. Fiorani, A.M. Testa, L. Suber, E. Agostinelli, M. Godinho, Phys. Rev. B 68 (2003) 212408.

[71] Ö. Özdemir, D.J. Dunlop, T.S. Berquó, Geochem. Geophys. Geosyst. 9 (2008) Q10Z01.

[72] R.E. Vandenberghe, A.E. Verbeeck, E. De Grave, W. Stiers, Hyperfine Interact. 29 (1986) 1157–1160.

[73] Ö. Helgason, I. Ayub, F.J. Berry, E. Crabb, Hyperfine Interact. 141 (142) (2002) 291–295.

[74] E. De Grave, D. Chambaere, L.H. Bowen, J. Magn. Magn. Mater. 30 (1983) 349–354.

[75] R.E. Vandenberghe, E. Van San, E. De Grave, G.M. da Costa, Czech. J. Phys. 51 (2001) 663–675.

[76] E. Kuzmann, S. Nagy, A. Vértes, Pure Appl. Chem. 75 (2003) 801–858.

[77] G.F. Goya, M. Veith, R. Rapalavicuite, H. Shen, S. Mathur, Appl. Phys. A 80 (2005) 1523–1526.

[78] S. Onari, T. Arai, K. Kudo, Phys. Rev. B 16 (1977) 1717–1721.

[79] C.J. Serna, J.L. Rendon, J.E. Iglesias, Spectrochim. Acta 38A (1982) 797–802.

[80] S. Hayashi, H. Kanamori, J. Phys. C Solid State 13 (1980) 1529–1538.

[81] C.J. Serna, M. Ocaña, J.E. Iglesias, J. Phys. C Solid State 20 (1987) 473–484.

[82] Y. Wang, A. Muramatsu, T. Sugimoto, Colloid Surf. A: Phys. Eng. Aspects 134 (1998) 281–297.

[83] L. Chen, X. Yang, J. Chen, J. Liu, H. Wu, H. Zhan, C. Liang, M. Wu, Inorg. Chem. 49 (2010) 8411–8420.

[84] S.A. Fysh, P.M. Fredericks, Clays Clay Miner. 31 (1983) 377–382.

[85] E. Van San, E. De Grave, R.E. Vandenberghe, H.O. Desseyn, L. Datas, V. Barrón, A. Rousset, Phys. Chem. Miner. 28 (2001) 488–497.

[86] J.L. Rendon, J. Cornejo, P. de Arambarri, C.J. Serna, J. Colloid Interface Sci. 92 (1983) 509–516.

[87] M.P. Morales, N.O. Nuñez, R. Pozas, M. Ocaña, C.J. Serna, Appl. Spectrosc. 56 (2002) 200–204.

[88] M. Žic, M. Ristić, S. Musić, J. Mol. Struct. 834–836 (2007) 141–149.

[89] S. Musić, S. Krehula, S. Popović, Mater. Lett. 58 (2004) 444–448.

[90] S. Musić, S. Krehula, S. Popović, Mater. Lett. 58 (2004) 2640–2645.

[91] D.M. Sherman, Phys. Chem. Miner. 12 (1985) 161–175.

[92] D.M. Sherman, T.D. Waite, Am. Mineral. 70 (1985) 1262–1269.

[93] B. Gilbert, C. Frandsen, E.R. Maxey, D.M. Sherman, Phys. Rev. B 79 (2009) 035108.

[94] Y.P. He, Y.M. Miao, C.R. Li, S.Q. Wang, L. Cao, S.S. Xie, G.Z. Yang, B.S. Zou, C. Burda, Phys. Rev. B 71 (2005) 125411.

[95] L. Lu, L. Li, X. Wang, G. Li, J. Phys. Chem. B 109 (2005) 17151–17156.

[96] J. Wang, W.B. White, J.H. Adair, J. Am. Ceram. Soc. 88 (2005) 3449–3454.

[97] H.M. Fan, G.J. You, Y. Li, Z. Zheng, H.R. Tan, Z.X. Shen, S.H. Tang, Y.P. Feng, J. Phys. Chem. C 113 (2009) 9928–9935.

[98] J. Štajdohar, M. Ristić, S. Musić, J. Alloys Compd. 532 (2012) 41–48.